CrossMark

JM PAPERS

Similarity of length scales in high-Reynolds-number wall-bounded flows

Nikolay Gustenyov[1], Margit Egerer[2], Marcus Hultmark[3], Alexander J. Smits[3] and Sean C.C. Bailey[1],†

[1]Department of Mechanical and Aerospace Engineering, University of Kentucky, Lexington, KY 40506, USA

[2]Department of Computer Systems, Tallinn University of Technology, Tallinn 12618, Estonia

[3]Department of Mechanical and Aerospace Engineering, Princeton University, Princeton, NJ 08544, USA

The wall dependence of length scales used to describe large- and small-scale structures of turbulence is examined using highly resolved experiments in zero-pressure-gradient turbulent boundary layers and pipe flows spanning the range $2000 < Re_\tau < 37\,700$. Of particular interest is the influence of external intermittency on the scaling of these length scales. It is found that when suitable scaling parameters are selected and external intermittency is accounted for, the dissipative motions follow inner scaling even into the outer-scaled regions of the flow, and that certain large-scale descriptions follow outer scaling even in the inner-scaled regions of the flow. The wall dependence is the same for both internal pipe and external boundary layer flows, and the different length scales can be related to recognizable features in the longitudinal wavenumber spectrum.

Key words: intermittency, pipe flow, turbulent boundary layers

1. Introduction

Due to their importance in numerous engineering and natural systems, the scaling of turbulent wall-bounded flows has been a subject of great interest (e.g. Coles 1956; Smits *et al.* 2011; Marusic *et al.* 2013). Close to the wall, the mean flow follows inner scaling, with a characteristic velocity scale called the friction velocity, $u_\tau = (\tau_w/\rho)^{-1/2}$, and a characteristic length scale called the viscous length scale, ν/u_τ, where τ_w is the wall shear stress, and ρ and ν are the density and kinematic viscosity of the fluid, respectively.

In the outer part of the flow, the statistics follow outer scaling, with the same velocity scale u_τ but a different length scale corresponding to the layer thickness δ. At high Reynolds numbers, an overlap region develops where both scalings are valid. These observations hold for pipe, channel and boundary layer flows, but the external boundary conditions produce some differences in the functional relationships among these flows in the outer region (that is, in the wake region).

The turbulent stresses generally follow this scaling behaviour, except that the large-scale motions in the outer and overlap regions interact with the small-scale motions in the inner region through time-dependent superimposition and amplitude modulation, so the amplitudes of the inner layer stresses display a Reynolds number dependence (e.g. Mathis, Hutchins & Marusic 2009; Marusic, Mathis & Hutchins 2010; Smits 2020; Smits *et al.* 2021). Nevertheless, the stresses all display a wide range of wavenumbers, and Kolmogorov (1941) proposed that at sufficiently large Reynolds number, the small scales of turbulence (the high wavenumber parts of the spectrum) are homogeneous and isotropic, and independent of boundary conditions, thereby having universal characteristics dictated only by the mean dissipation rate $\langle \varepsilon \rangle$ of turbulent kinetic energy, and ν. We use $\langle \cdot \rangle$ to indicate a mean quantity assessed over a statistically homogeneous ensemble. For the stationary and ergodic flows considered here, we determine $\langle \cdot \rangle$ using a time average that is thus dependent on spatial position. There is an intermediate range of wavenumbers, called the inertial subrange, where the power spectral density is independent of the viscosity and follows the famous $-5/3$ law. At the highest wavenumbers, in the dissipative range where viscosity is dominant, dimensional analysis of $\langle \varepsilon \rangle$ and ν yields the Kolmogorov length scale $\langle \eta_K \rangle = (\nu^3/\langle \varepsilon \rangle)^{1/4}$ and velocity scale $u_\eta = (\langle \varepsilon \rangle \nu)^{1/4}$. Kolmogorov scaling has been tested extensively in wall-bounded flows (e.g. Saddoughi & Veeravalli 1994) and found to successfully scale the dissipative motions, for example through the collapse of the high-wavenumber end of energy spectra scaled by $\langle \varepsilon \rangle$, ν and $\langle \eta_K \rangle$ (e.g. Grant, Stewart & Moilliet 1962; Rosenberg *et al.* 2013).

What has received less attention in wall-bounded flow is the wavenumber relationship between inner/outer scales, δ and ν/u_τ, and their commensurate scales $\mathcal{L}$ and $\langle \eta_K \rangle$, where $\mathcal{L}$ is a characteristic measure of the low-wavenumber end of the spectrum (e.g. Kolmogorov 1941; Pope 2000). Of interest here is the universality of this coupling among internal (pipe and channel) and external (turbulent boundary layer) flows. One of the challenges associated with our investigation is that the Reynolds number needs to be large enough to achieve sufficient separation of scales, so that $\delta \gg u_\tau/\nu$ and $\mathcal{L} \gg \langle \eta_K \rangle$.

Complicating any comparison between internal and external flows is the presence of intermittency in external flows, where laminar freestream fluid is entrained into the boundary layer along a time-dependent turbulent/non-turbulent interface (Kovasznay, Kibens & Blackwelder 1970). This interaction between turbulent and non-turbulent fluid, which is absent in fully-developed channel and pipe flows, occurs on two separate scales: one that is correlated with the size of the large-scale motions in the outer layer ($\sim 2\delta$–3δ), and one that is a diffusive, viscous scale at the interface itself (Kovasznay 1967). The first is called the entrainment scale, and the second is referred to as nibbling at the interface (Mathew & Basu 2002; Westerweel *et al.* 2005; Holzner *et al.* 2007). The level of intermittency varies strongly with the distance from the wall; near the wall, the flow is fully turbulent, while it is laminar in the freestream. Hence it can be expected that the presence of intermittency provides a strong influence on any locally averaged statistics calculated in the outer layer of external flows.

Here, we combine previously unpublished highly resolved experimental data from a high-Reynolds-number turbulent boundary layer with previously published well-resolved

high-Reynolds-number pipe and boundary layer measurement data to examine the relationship between different length scales of turbulence, with particular focus on the influence of external intermittency on the comparison between internal to external flows. The high Reynolds numbers of these data allows the conditions required for the formation of an inertial subrange, i.e. $\mathcal{L} \gg \langle \eta_K \rangle$, to be met. With these data, we show that properly selected small-scale turbulence descriptors follow inner scaling throughout the wall-bounded flow, including in regions expected to be described by outer scaling, and that properly selected descriptors of large-scale turbulence follow outer scaling throughout the wall-bounded flow. Similar behaviour was observed for both internal and external boundary layer flows, once rectification had been applied for the effects of external intermittency, and we show that these scales can be related to features in the longitudinal energy spectrum.

2. Experiments description

2.1. *Facilities and flow conditions*

The high-Reynolds-number wall-bounded flow data were acquired using thermal anemometry in three different facilities. Two data sets come from compressed-air facilities: the High Reynolds Number Test Facility (HRTF) at the Princeton University Gas Dynamics Lab, in which a zero-pressure-gradient turbulent boundary layer was developed along a smooth flat plate in a compressed-air wind tunnel (with the measurements described in Vallikivi, Hultmark & Smits 2015*b*); and the canonical pipe flow produced by the Superpipe facility at the Princeton University Gas Dynamics Lab (with the measurements described in Hultmark *et al.* 2012, 2013). These data are complemented by additional, previously unpublished measurements taken in the High Reynolds Number Boundary Layer Wind Tunnel (HRNBLWT) at the University of Melbourne, Australia, in which the turbulent boundary layer develops along the wind tunnel floor. The HRNBLWT facility is described in Nickels *et al.* (2007).

Experimental conditions are summarized in tables 1–3 for the HRNBLWT, HRTF and Superpipe, respectively. In this study, δ represents the radius and 99 % boundary layer thickness for the pipe and turbulent boundary layer cases, respectively. Note that for the HRNBLWT turbulent boundary layer data, the friction velocity was estimated using the Clauser approach using von Kármán constant 0.39, whereas for the HRTF data, multiple techniques were used to estimate u_τ (see Vallikivi *et al.* 2015*b*). For the Superpipe measurements, the friction velocity was determined from the pressure loss measured along a length of the pipe (Hultmark *et al.* 2013). It should be noted that some differences have been observed between the mean velocity profiles of the corrected Pitot data and those produced by the Hultmark *et al.* (2013) data, which may be due to uncertainty in the determined friction velocity (e.g. Bailey *et al.* 2014). The data set encompasses an order of magnitude of Reynolds number range $2000 \lesssim Re_\tau \lesssim 38\,000$ in pipe flow, and $2500 \lesssim Re_\tau \lesssim 17\,000$ for the turbulent boundary layer. The HRNBLWT measurements, having higher resolution than the HRTF measurements, also provide confidence that observations made are agnostic to both facility and sensor resolution.

2.2. *Instrumentation*

To achieve the spatial and temporal resolutions required to resolve near-Kolmogorov scales at these Reynolds numbers, a nanoscale thermal anemometry probe (NSTAP) was used for all cases (as described in Bailey *et al.* 2010; Vallikivi *et al.* 2011;

Parameter	Case 1	Case 2	Case 3
Symbol	□	□	□
Boundary layer thickness, δ (m)	0.275	0.249	0.251
External mean velocity, U_{ex} (m s^{-1})	11.0	16.8	21.0
Friction velocity, u_τ (m s^{-1})	0.37	0.56	0.68
$Re_\tau = \delta u_\tau / \nu$	6500	9000	11 000
Ambient pressure (kPa)	101	101	101
$\ell^+ = \ell u_\tau / \nu$	1.42	2.17	2.71

Table 1. Table of experimental conditions, HRNBLWT.

Parameter	Case 1	Case 2	Case 3	Case 4
Symbol	△	△	△	△
Boundary layer thickness, δ (m)	0.0274	0.0280	0.0287	0.0281
External mean velocity, U_{ex} (m s^{-1})	9.1	10.4	10.6	10.8
Friction velocity, u_τ (m s^{-1})	0.33	0.35	0.35	0.34
$Re_\tau = \delta u_\tau / \nu$	2600	5100	9500	17 000
Ambient pressure (kPa)	458	810	1499	2890
$\ell^+ = \ell u_\tau / \nu$	5.8	10	17	29

Table 2. Table of experimental conditions, HRTF.

Parameter	Case 1	Case 2	Case 3	Case 4	Case 5	Case 6
Symbol	○	○	○	○	○	○
Pipe radius, δ (m)	0.0648	0.0648	0.0648	0.0648	0.0648	0.0648
Centreline mean velocity, U_{cl} (m s^{-1})	11.7	12.1	10.0	11.1	12.3	12.2
Friction velocity, u_τ (m s^{-1})	0.46	0.46	0.37	0.38	0.40	0.38
$Re_\tau = \delta u_\tau / \nu$	2000	3300	5400	10 500	20 300	37 700
Ambient pressure (kPa)	101	169	345	651	1195	2382
$\ell^+ = \ell u_\tau / \nu$	1.8	3.1	5.0	9.7	19	35

Table 3. Table of experimental conditions, Superpipe.

Hultmark *et al.* 2012, 2013; Vallikivi & Smits 2014; Bailey & Witte 2016). These probes measured the streamwise, U_1, component of velocity. Here, we will use subscripts 1, 2, 3 to indicate streamwise, wall-normal and transverse directions, respectively.

The probe used in these experiments had a sensing element measuring $\ell = 60$ μm long by 2 μm wide by 100 nm thick. The resulting ℓ^+ values are provided in tables 1–3 for each case. Noting that the minimum $\langle \eta_K \rangle^+$ is 2–3, these ℓ^+ values indicate that the probes were smaller than the Kolmogorov scale for all HRNBLWT cases, and for $Re_\tau < 5000$ for the Superpipe cases. At the highest Re_τ measured, the probe was only at the same order of magnitude of $\langle \eta_K \rangle$ within the outer layer. In addition, Monkewitz (2022) noted that sensor blockage could influence statistics measured by the NSTAP when the probe was less than 300 μm from the wall. However, comparison of HRNBLWT and HRTF cases at matched Re_τ suggests that the reduced spatial resolution and increased potential for probe blockage

within the compressed-air facilities does not appear to have a significant impact on the statistics considered here.

In all cases, the NSTAP probes were operated using a Dantec Streamline anemometer with resistance overheat ratio 1.2. However, digitization frequencies ranged from 250 kHz for the HRNBLWT cases to 300 kHz for the HRTF and Superpipe cases, with corresponding analogue anti-aliasing low-pass filter frequencies 100 kHz. Calibration of the probes took place *in situ*, directly prior to, and following, each measurement run using a Pitot-static tube located outside the boundary layer or at the centreline of the pipe. For all cases, measurements were conducted at more than 40 positions in the wall-normal $y = x_2$ direction.

Due to the feedback circuit employed in constant-temperature anemometry, and sample rates exceeding the energy content of the turbulence, there was f^2 noise (Saddoughi & Veeravalli 1996) present in the data at high frequencies. Therefore, when post-processing the data, we assumed that the frequency at which the local gradient of spectra transitions from negative to positive indicates the point where instrumentation noise is of the same order as turbulent signal (Bailey *et al.* 2009). We eliminate frequency content above this point using an eighth-order low-pass digital Butterworth filter with cutoff frequency f_{cut}. The actual value of f_{cut} was a function of the signal-to-noise ratio and varied with measurement position, Reynolds number and facility. In all cases, it was determined to be higher than the frequency corresponding to the Kolmogorov time scale.

In addition, Taylor's frozen flow hypothesis was employed to translate temporal statistics into spatial statistics, after ensuring that ratio $|u_1|/\langle U_1 \rangle$ was sufficiently small (Taylor 1938; Meneveau & Sreenivasan 1991), where u_1 arises from Reynolds decomposition following $U_1 = \langle U_1 \rangle + u_1$. It was thus assumed that local mean velocity is the advective velocity of all turbulent length scales, giving an approximation of spatial separation $\Delta x_1 \approx \langle U_1 \rangle \Delta t$, where Δt is a time displacement. Generally, Taylor's frozen flow hypothesis provides a reasonable approximation for small scales of turbulence; however, it is understood that it introduces error in translating large scales (Zaman & Hussain 1981; del Álamo & Jiménez 2009).

2.3. *External intermittency detection*

Appearance of intermittent laminar regions interspersed with regions of turbulent flow is known to bias the probability density functions (PDFs) of local dissipative length scale η towards larger scales within the outer layer (Alhamdi & Bailey 2018), and a similar influence can be expected on other statistical quantities. Hence an external intermittency detection approach was used to distinguish instances when the probe was within turbulent flow from when it was in laminar flow. In previous work, identification of the turbulent–laminar interface within velocity time series was conducted using detection functions based on time derivatives of velocity components, instantaneous shear stress, velocity magnitude and local kinetic energy (Hedleyt & Keffer 1974; Tsuji *et al.* 1991; Chauhan *et al.* 2014). Here, the kinetic energy criterion was used to identify turbulent regions following the procedure developed by Chauhan *et al.* (2014). This approach assumes that within the outer region of a turbulent boundary layer, non-turbulent regions have an advective velocity close to the external flow velocity U_{ex}, while turbulent regions originating from the wall will have mean velocity that is lower than U_{ex} (Corrsin & Kistler 1955; Fiedler & Head 1966; Kovasznay *et al.* 1970; Jiménez *et al.* 2010;

Chauhan *et al.* 2014). This allows the formation of the detection function

$$\gamma(t) = 100 \left(1 - \frac{U_1(t)}{U_{ex}}\right)^2, \tag{2.1}$$

such that, when combined with a threshold value, the region is assumed to be non-turbulent when $\gamma(t)$ is less than the threshold. Previous experimental work showed that in case of the external boundary layer, the freestream turbulence intensity is not exactly zero, in contrast to jet flows, thus selecting correct threshold value can be challenging (Chauhan *et al.* 2014). Here, the threshold value $\gamma_t = 0.05$ was used, which corresponds to $|u_1| \approx 0.02U_{ex}$ at the edge of the boundary layer.

Using this indicator, statistics could be extracted from only the turbulent regions detected within the time series. Note that external intermittency was most evident for $y/\delta \gtrsim 0.5$, increasing in frequency with y, and reaching a maximum frequency at $y \approx 0.7\delta$. For $y > 0.8\delta$, external laminar flow was predominant, which meant that the average length of laminar regions became larger than the average length of turbulent regions. Hence as y approached δ, some individual turbulent regions were found to become too short to achieve converged statistics. To address this issue, the minimum size of turbulent regions considered was set at half the boundary layer thickness. This value ($\gtrsim 0.5\delta$) was selected for two reasons: (1) it was found to be the minimum value that allowed calculation of acceptable energy spectra; and (2) it ensured that the lengths of the shortest turbulent regions were of the order of the wall-normal distance and/or the boundary layer thickness. For the purpose of the current paper, small-scale nibbling motions around the interface were assumed to be a part of the turbulent structure, therefore only larger-scale motions ($\approx O(\delta)$, as suggested by Chauhan *et al.* 2014) were considered in separating turbulent/non-turbulent flows. However, it was found that effects of including short regions in deriving the statistics were insignificant for the range $0.5\delta \lesssim y \lesssim \delta$.

Finally, when calculating point statistics requiring an advective velocity, the advective velocity used was the global mean value of all the turbulent regions. This was done to account for contributions to the local fluctuations from the different advective velocities of each turbulent region. Conversely, to avoid biases by the interfaces when calculating time-dependent statistics, these were calculated using the advective velocity for the individual turbulent regions and then ensemble averaged. For example, to evaluate the energy spectrum at a wall-normal distance within the region influenced by external intermittency, the spectrum was calculated for each portion of the time series identified as turbulent, and then interpolated to a common wavenumber vector prior to averaging.

3. Results

3.1. *Large scales*

We begin by examining the scaling of parameters used to characterize large and most energetic scales of turbulence, $\mathcal{L}$. In practice, the integral length scale *ILS* is often used as a measure of $\mathcal{L}$, to represent the low wavenumber end of the inertial subrange (or the beginning of the $-5/3$ region). To calculate *ILS*, we used Taylor's hypothesis and integrated the autocorrelation following

$$ILS = \frac{\langle U_1 \rangle}{\langle u_1^2 \rangle} \int_0^{\tau_c} \langle u_1(t + \tau)u_1(t) \rangle \, \mathrm{d}\tau, \tag{3.1}$$

where τ_c is the value of τ where the autocorrelation first reaches value 0.

Wall-bounded turbulent flow has large-scale anisotropic structures that will influence *ILS*, which here is calculated using the longitudinal velocity component only. These structures include sublayer streaks (Kline *et al.* 1967), hairpin vortices near the wall (Head & Bandyopadhyay 1981), large-scale motions corresponding to bulges of turbulence at the edge of the wall layer (Kim & Adrian 1999; Guala, Hommema & Adrian 2006; Balakumar & Adrian 2007), and superstructures of very large scale within the overlap region and, in the case of pipe and channel flows, within the wake region as well (Kim & Adrian 1999; Hutchins, Hambleton & Marusic 2005; Monty 2005; Tomkins & Adrian 2005; Guala *et al.* 2006; Balakumar & Adrian 2007; Monty *et al.* 2009). Large-scale motions also modulate the near-wall flow and influence the flow structure near the wall (Mathis *et al.* 2009). Considering the various length scales of these energy-containing motions, the *ILS* value can be expected to represent a superposition of a range of anisotropic contributions, and therefore may not be an appropriate metric to exemplify the idealized isotropic eddies below the low-wavenumber end of the inertial subrange. Within wall bounded flows, it has also been suggested that the energy-containing range of the spectrum depends on δ, with an overlap inertial layer scaling with y (Perry, Henbest & Chong 1986; Morrison *et al.* 2004; Vallikivi, Ganapathisubramani & Smits 2015*a*).

An alternative approach to describe $\mathcal{L}$, which can be used when there is no clear geometric large scale, can be found from scaling arguments based on the energy cascade, specifically

$$\mathcal{L} = \frac{TKE^{3/2}}{\langle \varepsilon \rangle}, \tag{3.2}$$

where *TKE* is the turbulent kinetic energy.

However, (3.2) requires estimation of both mean dissipation rate $\langle \varepsilon \rangle$ and turbulent kinetic energy *TKE*. As the NSTAP was unable to resolve more than one component of velocity, we instead use the approximation

$$L \approx \frac{\left(\frac{3}{2} \langle u_1^2 \rangle \right)^{3/2}}{\langle \varepsilon \rangle}. \tag{3.3}$$

Note that due to the anisotropy of wall-bounded turbulence, $\frac{3}{2} \langle u_1^2 \rangle$ should not be considered to be an accurate estimate of *TKE*. Furthermore, $\langle u_1^2 \rangle$ is itself subject to contributions from longitudinal energetic structures, hence their contribution cannot be neglected, and *L* should be considered as an estimate of the longitudinal scale of the large eddies. When examining the scaling of dissipative motions at low Re_τ (Alhamdi & Bailey 2017, 2018), this measure of the longitudinal length scale provided reasonable scaling of fine turbulent structure within the boundary layer for the entire range of y, once external intermittency was accounted for.

The mean dissipation rate $\langle \varepsilon \rangle$ was found assuming local isotropy and integrating the one-dimensional dissipation spectrum $D(k_1)$ (Townsend 1976). This, in turn, was approximated by the one-dimensional longitudinal energy spectrum $E_{11}(k_1)$ such that

$$\langle \varepsilon \rangle \approx \int_0^{k_c} D(k_1) \, dk_1 \approx 15\nu \int_0^{k_c} k_1^2 E_{11}(k_1) \, dk_1, \tag{3.4}$$

where the streamwise wavenumber was found from frequency f according to $k_1 \approx 2\pi f/\langle U_1 \rangle$. Note that k_c is the wavenumber representation of the filter frequency f_{cut}. For $y^+ > 50$, comparison of $\langle \varepsilon \rangle$ calculated using this approach by Bailey & Witte (2016) in channel flow was found to compare favourably to the $\langle \varepsilon \rangle$ values calculated from the

direct numerical simulation data of Lee & Moser (2015) at similar Reynolds numbers. The reduced agreement for $y^+ < 50$ can be attributed to the reduced scale separation and increased anisotropy of the small scales near the wall. Similar behaviour can be expected in the current data set.

It was found that the HRTF data had under-resolved high-frequency content due to low signal-to-noise ratio at the high frequency. Therefore, to obtain estimates of $\langle \varepsilon \rangle$ for these cases, the longitudinal energy spectrum scaling was assumed, allowing a fit to the inertial subrange such that

$$\langle \varepsilon \rangle \approx \left(\frac{1}{C_1} k_1^{5/3} E_{11}(k_1) \right)^{3/2} , \tag{3.5}$$

using $C_1 = 0.53$ as suggested by Sreenivasan (1995).

Although both *ILS* and *L* have been identified as potential characteristic longitudinal length scales of the energy containing eddies, which are expected to scale with δ, comparison of the outer-scaled behaviour between the two, as done in figure 1, shows significant differences in their scaling behaviours. Figure 1(*a*) reveals that despite there being collapse of ILS/δ for $y/\delta < 0.05$, for $y/\delta > 0.05$ there is both Reynolds-number-dependent and geometry-dependent variability observed. Although $ILS \approx \delta$ for $y/\delta > 0.1$, the profiles of L/δ shown in figure 1(*b*) show larger values with $L \approx 1.5\delta$–2.5δ. Hence, with increasing *y*, the values of *L* are larger than *ILS* for $y/\delta > 0.5$, although neither appears to capture the scale of large-scale (2δ–3δ) or very-large-scale (10δ–20δ) motions.

For both ILS/δ and L/δ, the boundary layer cases show higher Reynolds number dependence than the pipe flow cases for all $y < \delta$. Notably, this behaviour changes significantly when only the turbulent regions of the outer layer are considered when calculating these scales, as shown in figures 1(*c*) and 1(*d*) for ILS/δ and L/δ, respectively. From figure 1(*c*), it is evident that the Reynolds number dependence of ILS/δ for the boundary layer is reduced significantly, and two clear trends appear, differentiating the pipe and boundary layer flow behaviours. The decrease in ILS/δ evident with increasing y/δ is consistent with the wall-normal structure of the uniform momentum zones observed in turbulent boundary layers (de Silva, Hutchins & Marusic 2016).

Interestingly, as shown in figure 1(*d*), there is an increased agreement between pipe and boundary layer cases in the wall-normal dependence of L/δ (in the range $0.05 < y \le \delta$) once the boundary layer cases have been corrected for external intermittency. Note that variability in the L/δ scaling for $y/\delta < 0.05$ could be attributed to the approximations used to estimate $\langle \varepsilon \rangle$. The improvement in agreement further from the wall suggests that much of the differences between the two geometries in the outer layer can be attributed to external intermittency. One possible explanation for this reduced geometry dependence is that *L*, being composed of $\langle u_1^2 \rangle$ and $\langle \varepsilon \rangle$, will be modulated by the isotropy of $\langle \varepsilon \rangle$, and much more tightly bounded by *y* than *ILS* which, as discussed previously, can include increased contributions from anisotropic large scales.

This last observation is further highlighted by comparing the $ILS/\langle \eta_K \rangle$ and $L/\langle \eta_K \rangle$ Reynolds number dependence which, following classical scaling arguments, is expected to follow $Re_{ILS}^{3/4}$ or $Re_L^{3/4}$ behaviour, respectively. Here, $Re_{ILS} = \langle |\Delta_{ILS}| \rangle \, ILS/\nu$ and $Re_L = \langle |\Delta_L| \rangle \, L/\nu$, where

$$\Delta_\tau = u_1(t + \tau) - u_1(t), \tag{3.6}$$

is the longitudinal velocity increment, and $|\tau|$ is equal to $ILS/\langle U_1 \rangle$ and $L/\langle U_1 \rangle$ for Δ_{ILS} and Δ_L, respectively.
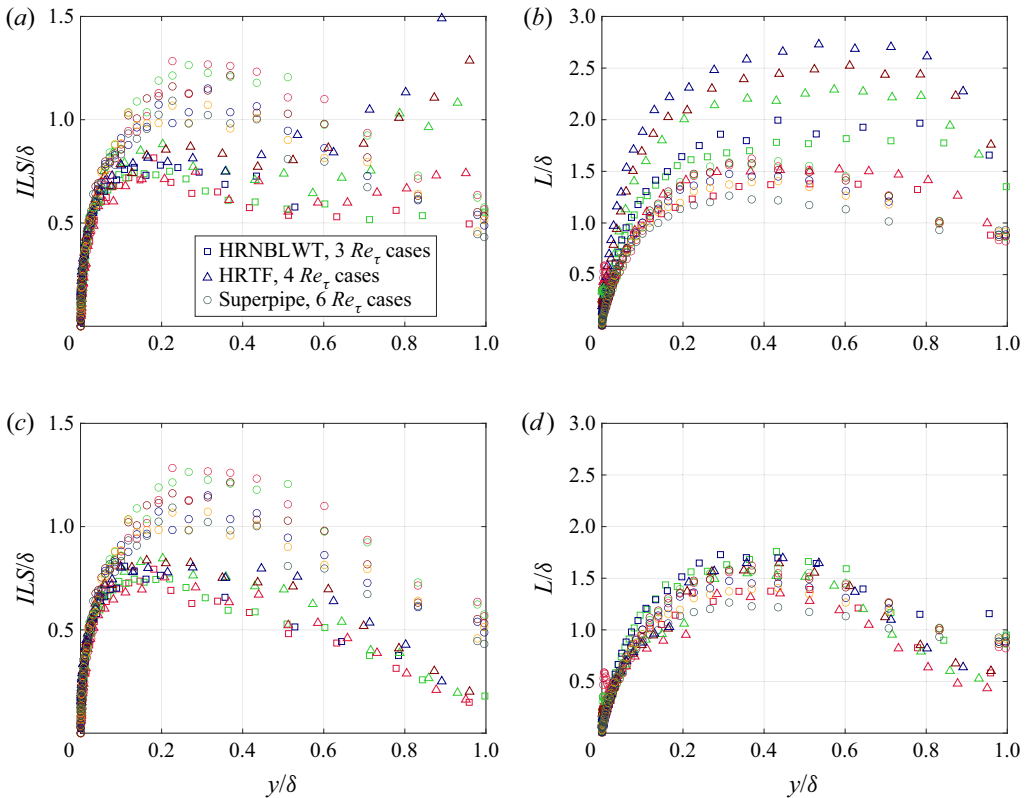
Figure 1. Outer-scaled (*a*) *ILS* and (*b*) *L*, including laminar portions of the time series in the *ILS* and *L* calculation. Corresponding outer-scaled profiles using only turbulent portions of the time series in the calculation are shown in (*c*) *ILS* and (*d*) *L*. All cases are shown with symbols as provided in tables 1–3.

In figures 2(*a*,*b*), we compare the scaling of $ILS/\langle \eta_K \rangle$ as a function of Re_{ILS} to the scaling of $L/\langle \eta_K \rangle$ as a function of Re_L. Although both descriptions of the large scales produce trends close to the expected 3/4 exponent, the $ILS/\langle \eta_K \rangle$ scaling shows more variability about the slope. Although it is not strictly clear in figure 2(*a*), at high Re_{ILS} a single profile can produce multiple values of $ILS/\langle \eta_K \rangle$ for the same value of Re_{ILS}. This is best illustrated in figure 2(*c*), which isolates the single case of pipe flow at $Re_\tau = 10\,500$.

Conversely, $L/\langle \eta_K \rangle$ (see figure 2*b*) has much more consistent agreement with the theoretical 3/4 slope, and little evidence of non-uniqueness in the Re_L dependence. Figure 2(*d*) shows this behaviour for the isolated pipe flow case at $Re_\tau = 10\,500$. However, for $Re_L > 10^3$, the local slope of $L/\langle \eta_K \rangle$ deviates from $Re_L^{3/4}$ and becomes closer to $Re_L^{0.76}$. Note that the agreement of the $L/\langle \eta_K \rangle$ scaling is not unexpected as $\langle \eta_K \rangle \sim L Re_L^{-3/4}$ can be recovered exactly by replacing Δ_L with $\langle u_1^2 \rangle^{1/2}$ as the velocity scale in Re_L. Therefore, the deviation from 3/4 slope in figure 2(*b*) reflects the difference between $\langle u_1^2 \rangle^{1/2}$ and Δ_L as representative velocity scales associated with *L*. However, since $\langle u_1^2 \rangle^{1/2}$ is an integrated quantity over all scales, it is less descriptive of the largest scales, therefore it makes heuristic sense to use Δ_L as a description of the large-scale turbulence as it is linked directly to the energy at spatial scale *L*. There is also deviation of $L/\langle \eta_K \rangle$ from 3/4 slope at $Re_L < 200$, which can be attributed to insufficient scale separation.
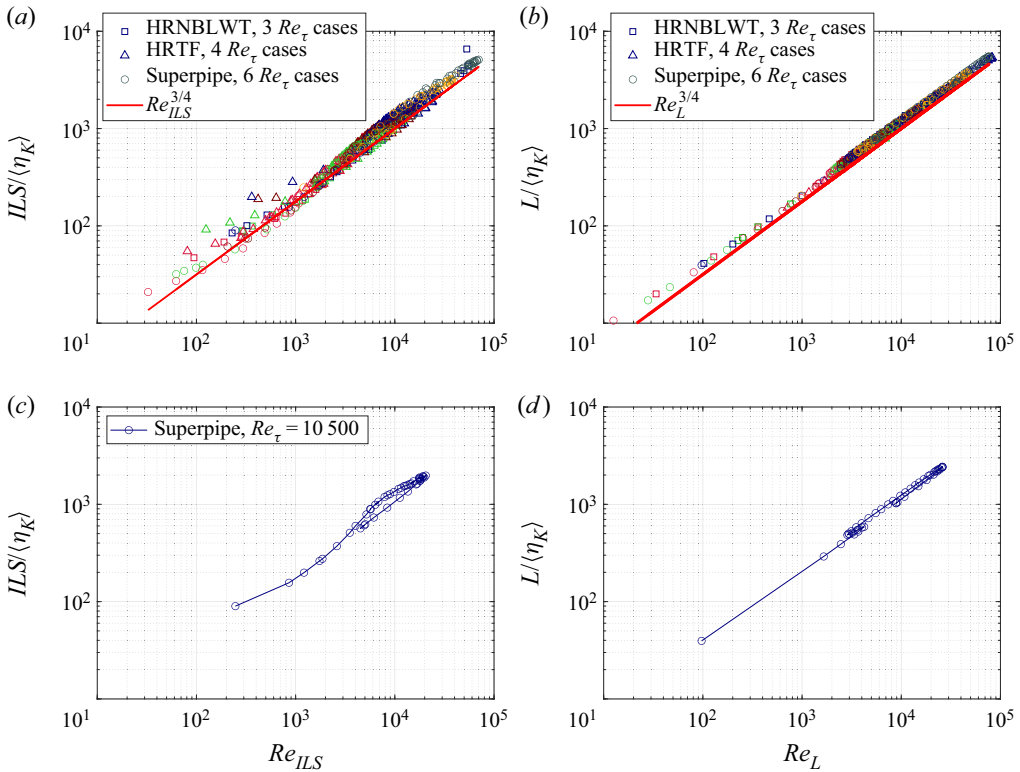
Figure 2. Scale separation represented by (*a*) $ILS/\langle\eta_K\rangle$ and (*b*) $L/\langle\eta_K\rangle$ as functions of Re_{ILS} and Re_L, respectively. The same results isolated for a single case of pipe flow at $Re_\tau = 10\,500$ are shown in (*c*) and (*d*), respectively. Symbols as provided in tables 1–3, with a red line indicating $Re_{ILS}^{3/4}$ in (*a*), and $Re_L^{3/4}$ in (*b*). External intermittency effects are accounted for in both (*a*) and (*b*).

To summarize, the comparison of *ILS* to *L* as a characteristic measure of the longitudinal large length scale of wall-bounded turbulent flow demonstrates that *L* exhibits significantly less dependence on Re_τ and geometry. There are two potential reasons for this result. First, in fixed-point measurements, calculation of *ILS* requires assuming that Taylor's frozen flow hypothesis is valid at large scales. It has long been acknowledged that Taylor's hypothesis can bias large-scale statistics (e.g. del Álamo & Jiménez 2009). Conversely, the calculation of *L* requires the Taylor's hypothesis to be valid only at small scales, which is a more reasonable assumption, at least farther from the wall ($y^+ > 50$). Second, since *ILS* is a superposition of a wide range of large length scales, it is influenced by external intermittency. Even when a correction is imposed (e.g. (2.1)), the correction effectively high-pass filters integral statistics by segmenting the turbulent regions into smaller ensembles, which reduces the measured longitudinal scale. In contrast, *L*, being a point statistic (which can also be calculated in the statistically homogeneous spanwise and azimuthal directions), displays greatly reduced Re_τ and geometry dependence once external intermittency corrections have been applied.

3.2. *Small scales*

We now examine the effect of external intermittency on the scaling of the smallest, dissipative motions of turbulence. To do so, we examine not just the scaling of the
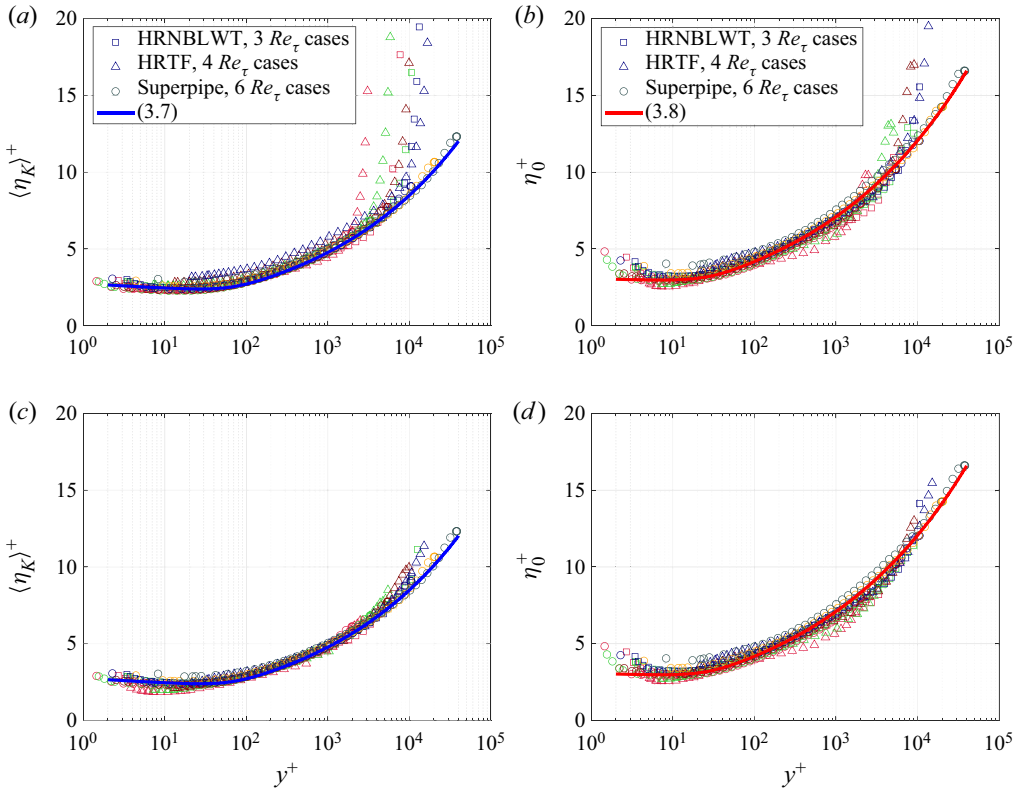
965 A17-10

Figure 3. Inner-scaled (*a*) $\langle \eta_K \rangle$ and (*b*) η_0, including laminar portions of the time series in the $\langle \eta_K \rangle$ and η_0 calculations. Corresponding inner-scaled profiles using only turbulent portions of the time series in the calculation are shown in (*c*) $\langle \eta_K \rangle$ and (*d*) η_0. All cases are shown with symbols as provided in tables 1–3. Blue lines indicate (3.7), and red lines indicate (3.8).

Kolmogorov scale $\langle \eta_K \rangle$, but also an alternative descriptor η_0, introduced to account for internal intermittency (Yakhot 2006; Hamlington *et al.* 2012*a*; Schumacher *et al.* 2014). This length scale, defined as $\eta_0 \sim L Re_L^{-0.73}$, can be considered as analogous to $\langle \eta_K \rangle$, but intrinsically enforces the scaling presented in figure 2. We first examine the inner-scaled behaviour of these parameters using figure 3, which shows $\langle \eta_K \rangle^+ = \langle \eta_K \rangle u_\tau / \nu$ and $\eta_0^+ = \eta_0 u_\tau / \nu$ as functions of inner-scaled wall-normal distance $y^+ = y u_\tau / \nu$.

The quantities $\langle \eta_K \rangle$ and η_0 represent two approaches to quantify the dissipative scales, and as shown in figures 3(*a,b*), both of these metrics for the small scales exhibit inner scaling in the near-wall region for both geometries over a wide range of Reynolds numbers, with $\langle \eta_K \rangle^+$ exhibiting better agreement than η_0^+. Notably, the pipe flow results exhibit collapse over the entire range of y^+ values, whereas the turbulent boundary layer results exhibit Re_τ dependence in the outer layer. This last observation is shown to be a consequence of external intermittency as demonstrated by figures 3(*c,d*), which reveals that once external intermittency was accounted for, both parameters scale well using inner scaling over the entire depth of the wall-bounded flow over a large Reynolds number range and independent of boundary conditions. That said, figure 3(*c*) does show some residual outer-layer dependence, with deviations from the general trend less than 20 %.

965 A17-11

Similar outer-layer dependence was noted in the lower-Reynolds-number channel flow measurements of Bailey & Witte (2016).

Note that $\langle \eta_K \rangle^+$ and η_0^+ are of the same order, and both show dependence on y^+, which can be expected given the change in local turbulence Reynolds number and corresponding wall-distance-dependent scale separation within the turbulence. However, a slightly different relationship with y^+ can be observed between the two, as could be expected from the different Re_L behaviours for these two parameters.

For $y^+ \geq 10$, the wall-normal dependencies of both $\langle \eta_K \rangle^+$ and η_0^+ were well represented by empirical power-law approximations

$$\langle \eta_K \rangle^+ \approx 0.85(y^+)^{0.25} \coth \left(\frac{y^+}{50} \right)^{0.3} \tag{3.7}$$

and

$$\eta_0^+ \approx 1.45(y^+)^{0.23} \coth \left(\frac{y^+}{20} \right)^{0.25}, \tag{3.8}$$

where the hyperbolic cotangent is introduced as a damping function to represent the increased influence of viscosity near the wall (see figure 3).

Both dissipation rate and scales have also been understood to have spatially intermittent behaviour, where regions of intensive dissipation are separated by regions of lower turbulent dissipation rate (Batchelor & Townsend 1949). This internal intermittency suggests that the mean dissipation rate, and by extension $\langle \eta_K \rangle$, may be a poor representation of the highly skewed dissipation field (Schumacher *et al.* 2014). Instead, it has been proposed that treating dissipation as a random fluctuating field introduces the potential for improved scaling of small-scale statistics at higher-order moments (Yakhot 2006; Yakhot, Bailey & Smits 2010).

By treating the dissipation scale as a fluctuating field of local dissipation scales, it is then characterized using a distribution of dissipative scales. This distribution can be obtained for the Kolmogorov scales by utilizing the intermittent distribution of dissipation rate. Time series of instantaneous dissipation rate can be approximated using

$$\varepsilon(t) \approx \frac{15\nu}{\langle U_1 \rangle^2} \left(\frac{\mathrm{d}u_1}{\mathrm{d}t} \right)^2 . \tag{3.9}$$

In turn, the time dependence of the local Kolmogorov scale can be formed from

$$\eta_K(t) \approx \left(\frac{\nu^3}{\varepsilon(t)} \right)^{1/4}, \tag{3.10}$$

allowing a probability density function (PDF) of $\eta_K(t)$ to be calculated from each measured time series.

The resulting PDFs $Q(\eta_K / \langle \eta_K \rangle)$ are presented in figure 4(*a*) for all data sets considered here, including all Re_τ and wall-normal distances, totaling 552 time series.

The PDFs shown in figure 4(*a*) are analogous to the moments of the dissipation rate $\varepsilon^n / \langle \varepsilon \rangle^n$ presented in Hamlington *et al.* (2012*a*,*b*) and Schumacher *et al.* (2014), who observed universality in the *Re* dependence of these moments for homogeneous isotropic turbulence, the centreline of turbulent channel flow and the centre of Rayleigh–Bénard convection cells – locations where mean shear is minimal. However, they also observed that mean shear affects the PDF of local dissipation scales at low *Re*. Figure 4(*a*) shows that although the same general distribution is observed for the different Re_τ and
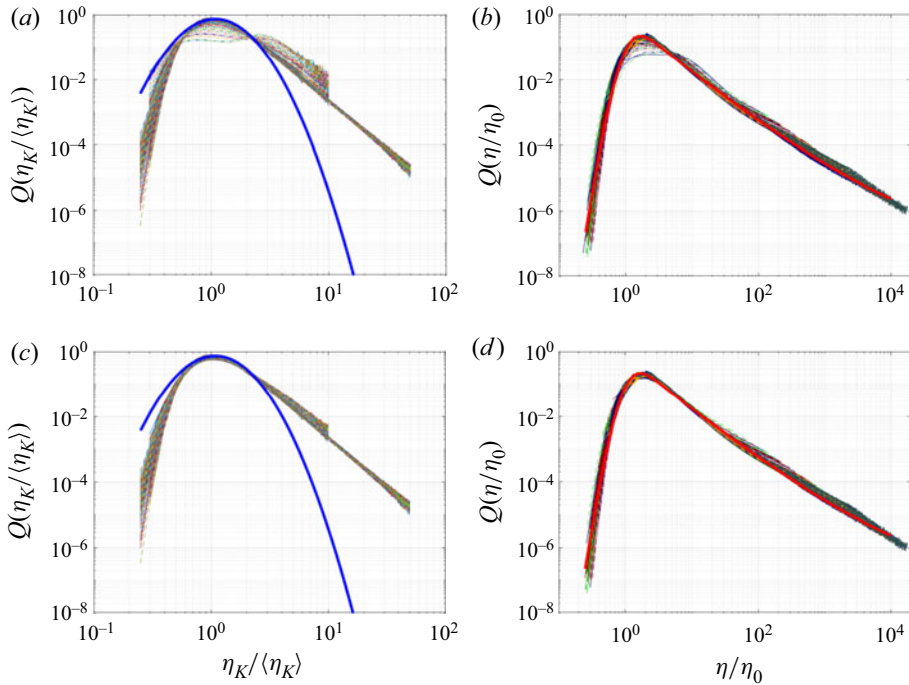
Figure 4. PDFs of (*a*) η_K and (*b*) η shown normalized, including laminar portions of the time series. Corresponding PDFs considering only turbulent portions of the time series are shown for (*c*) η_K and (*d*) η. All measurement locations for all cases measured are shown. The solid blue line is a log-normal distribution with mean $0.28\langle\eta_K\rangle$ and standard deviation $0.45\langle\eta_K\rangle$. The solid red line shows the empirical fit given by (3.12).

wall-normal positions (i.e. mean shear) considered here, there is significant variability in the distributions.

Alternative approaches to describing the dissipative scales have also been proposed (Paladin & Vulpiani 1987). For example, one possibility is to define a local dissipation scale η using the velocity increment (3.6) such that Δ_τ is found with $|\tau| = \eta/\langle U_1 \rangle$ (Yakhot 2006; Schumacher, Sreenivasan & Yakhot 2007). The definition of a dissipation scale is therefore an event where

$$\eta\,|\Delta_\eta| \approx \nu. \tag{3.11}$$

This is equivalent to identifying instances where the local Reynolds number is of order unity, i.e. $Re_\eta = \eta\Delta_\eta/\nu = O(1)$. When normalized by the scaling parameter η_0, the PDFs obtained from high-resolution direct numerical simulations data of homogeneous and isotropic turbulence as well as turbulent channel flows (Bailey *et al.* 2009; Hamlington *et al.* 2012*a*; Bailey & Witte 2016) were found to be in good agreement. The equivalent PDFs $Q(\eta/\eta_0)$ for the experiments considered here were found following the procedure described in Bailey & Witte (2016). Specifically, for each time series, for all t, Δ_τ was calculated where the time step τ was calculated using Taylor's hypothesis as $\tau = \eta/\langle U_1 \rangle$. Then instances where $0.5 \leq Re_\eta \leq 2$ were identified and counted to obtain a numerical distribution $P(\eta)$ over the range $0 < \eta < 4L$. The PDFs were then found from $P(\eta)$ by normalization, such that $Q(\eta) = \int_0^{4L} P(\eta)\,\mathrm{d}\eta = 1$.

The resulting PDFs are shown in figure 4(*b*) and take the form of a highly skewed distribution, with a peak at $\eta \approx 2\eta_0$, indicating that dissipation can occur at scales

much larger than η_0, including at energy-producing scales. Notably, there is much less scatter in the distributions, although some variability can be observed and attributed to the outer-layer regions of the boundary layer cases. This variability was attributed previously to the presence of external intermittency by Alhamdi & Bailey (2018), and when external intermittency is accounted for, as shown in figure 4(*d*), there is significantly better agreement between all Re_τ, wall-distance and geometries considered here.

Furthermore, when the PDFs $Q(\eta_K/\langle\eta_K\rangle)$ are also calculated accounting for the presence of external intermittency, the variability in the resulting distributions is also significantly reduced, although there is still some higher-order variability evident. This is illustrated by the distributions in figure 4(*c*) being well approximated for $\eta_K \approx \langle\eta_K\rangle$ by a log-normal distribution with mean $0.28\langle\eta_K\rangle$ and standard deviation $0.45\langle\eta_K\rangle$. Note that at the tails of $Q(\eta_K/\langle\eta_K\rangle)$, additional noise was evident due to limited instrumental sensitivity for these small velocity differences (i.e. for large values of η_K, the local dissipation rate ε, and thus velocity difference, must be small).

Clear differences in the distribution of dissipation scales appear between the approaches used in figures 4(*c*) and figure 4(*d*). The $Q(\eta_K/\langle\eta_K\rangle)$ distributions are noticeably less skewed, with much more concentration at smaller scales than the corresponding $Q(\eta/\eta_0)$ distributions. Both approaches demonstrated good collapse of PDFs, with peaks at $\langle\eta_K\rangle$ and $2\eta_0$, respectively, representing a factor of 3 difference in the most probable length scale (as indicated by figure 3).

Furthermore, as noted previously, $Q(\eta/\eta_0)$ shows good collapse over the entire range of η/η_0, while $Q(\eta_K/\langle\eta_K\rangle)$ has better agreement for the peak of the PDF. Similar observations of universality of these distributions have been made previously, although previous measurements of $Q(\eta/\eta_0)$ were limited to relatively low Reynolds numbers (Bailey *et al.* 2009; Zhou & Xia 2010; Hamlington *et al.* 2012*a*; Morshed, Venayagamoorthy & Dasi 2013; Alhamdi & Bailey 2017).

Finally, it was also found that the structure of $Q(\eta/\eta_0)$ over the range $1/4 \le \eta/\eta_0 \le 10^4$ could be well approximated by the empirical function

$$Q(\eta/\eta_0) \approx \frac{12^{(\eta/\eta_0)^{0.13}} \tanh{(1.3\eta/\eta_0)}^{15}}{16(\eta/\eta_0)^2}, \tag{3.12}$$

as shown in figure 4(*d*). Hence (3.8) and (3.12) can be combined to yield the distribution of dissipative scales over a very large Reynolds number range and over all distances from the wall.

3.3. *Additional length scales*

The length scales $\langle\eta_K\rangle$ and η_0 describe the smallest dynamically important scales of turbulence. However, the majority of turbulent kinetic energy dissipation occurs at scales significantly larger than $\langle\eta_K\rangle$ and η_0 (as illustrated in figure 4, for example).

In many cases, Taylor's microscale λ_f is often used as a proxy to describe the largest length scale at which viscous forces are relevant. In other words, it is used to describe the high-wavenumber end of the inertial subrange, at which dissipation starts becoming significant. This is consistent with Taylor's microscale being an intermediate length scale ($\mathcal{L} > \lambda_f > \langle\eta_K\rangle$). Following the comparison of the large- and small-scale descriptors between the external and internal flows, we can also examine the scaling of λ_f. Here, the longitudinal Taylor's microscale was calculated using the isotropic assumptions required
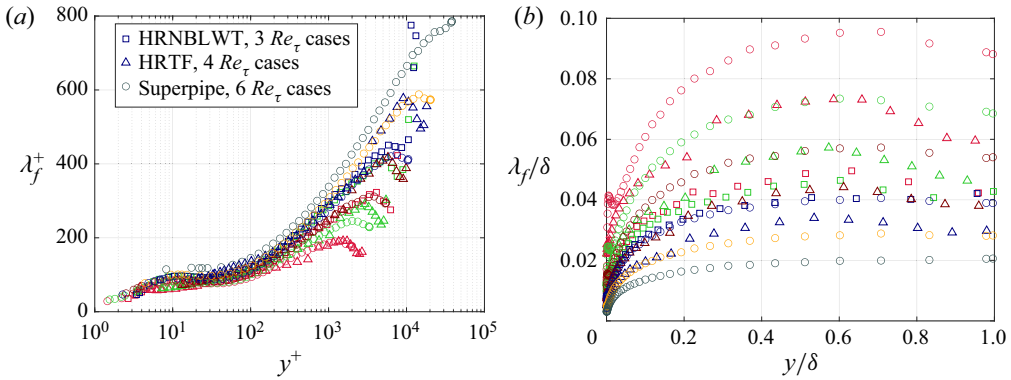
Figure 5. (*a*) Inner-scaled and (*b*) outer-scaled longitudinal Taylor's microscale λ_f. All cases are shown with symbols as provided in tables 1–3.

for the current data sets such that

$$\lambda_f \approx \left(\frac{30\nu\langle u_1^2 \rangle}{\langle \varepsilon \rangle} \right)^{1/2}. \tag{3.13}$$

Due to anisotropy in the Reynolds stresses, this approximation will likely result in an overestimation of the Taylor microscale.

As can be seen in figures 5(*a*,*b*), λ_f does not follow either inner or outer scaling, deviating from inner scaling for $y^+ > 100$, and showing no sign of collapse of the data in outer scaling. This can be attributed to the mixed-scale nature of λ_f, formed from $\langle u_1^2 \rangle$, which broadly follows outer scaling for $y/\delta > 0.02$ (Hultmark *et al.* 2013), and $\langle \varepsilon \rangle$, which, as demonstrated by figure 3(*c*), can be expected to follow inner scaling for most of the range $y < \delta$. Note that following the discussion in the previous subsection, the calculation has already accounted for the effects of external intermittency.

As an alternative to λ_f for describing the length scales at which the majority of turbulent kinetic energy dissipation is occurring, we can instead introduce a length scale L_ε corresponding to the wavenumber at which the peak of the premultiplied dissipation spectrum occurs, i.e. the wavenumber at which $15\nu k_1^3 E_{11}(k_1)$ is a maximum. This peak is then $2\pi/L_\varepsilon$, and represents the scales with the largest contribution to turbulent dissipation, following (3.4).

As shown in figure 6(*a*), this scale closely follows inner scaling for a wide range of Re_τ for all three data sets, and is consistent with the scaling of $\langle \eta_K \rangle^+$ shown in figure 3(*c*). For $y^+ > 50$, where small-scale homogeneous and isotropic assumptions are expected to be valid, L_ε can be approximated by $L_\varepsilon \approx 31\langle \eta_K \rangle$.

Comparing figures 5(*a*) and 6(*a*), λ_f and L_ε are of the same order of magnitude and almost identical at $y^+ \approx 50$. However, as the Reynolds number increases with wall-normal distance, the agreement between the two scales disappears, and λ_f^+ becomes Re_τ- and y-dependent.

To assess the relative importance of viscous forces at L_ε, it is possible to define a local Reynolds number $Re_{L_\varepsilon} = \Delta_{L_\varepsilon} L_\varepsilon / \nu$, where Δ_{L_ε} is the velocity increment from (3.6) with $|\tau| = L_\varepsilon/\langle U_1 \rangle$. This Reynolds number therefore describes the ratio of inertial forces to viscous forces at scales corresponding to L_ε. Figure 6(*b*) shows Re_{L_ε} as a function of y^+. Interestingly, Re_{L_ε} is constant near a value of 100 for both

965 A17-15
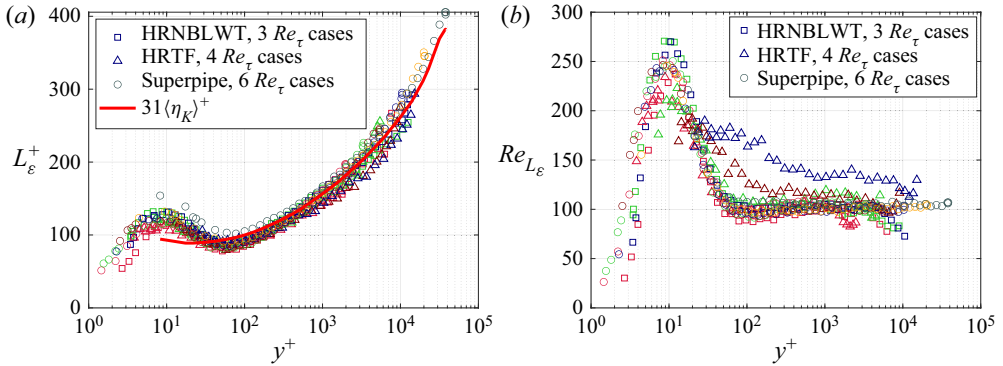
Figure 6. Profiles of (*a*) inner-scaled dissipation peak length scale L_ε and (*b*) Re_{L_ε} as functions of y^+. The solid red line in (*a*) shows (3.7) multiplied by a factor of 31. All cases are shown with symbols as provided in tables 1–3.

Superpipe and HRNBLWT flows for $y^+ > 50$ for all Re_τ, with the exception of the two highest Reynolds number HRTF cases, in which the calculation of the dissipation spectrum was found to be more challenging due to the presence of high-frequency noise.

Noting that L_ε is the scale where turbulence undergoes the highest rate of dissipation, this suggests that dissipation occurs when viscous effects are 1 % of inertial effects. For $y^+ < 50$, both pipe and boundary layer profiles follow the same trend, forming a peak for $Re_{L_\varepsilon} \approx 250$ at $y^+ \approx 10$. This is believed to be due to the fact that despite the peak production occurring in this y^+ range, the local Re_L value is relatively small, and there is insufficient separation of scales, resulting in increased inertial eddies occurring at the dissipation scales.

As the scaling of the large-scale turbulence in the boundary layer was found to be impacted significantly by the presence of external intermittency, it therefore becomes of interest to also examine the wavelength of the external intermittency and evaluate how this wavelength might be related to the underlying large-scale motions.

The intermittency detection approach described in § 2.3 provides a consistent way of detecting turbulent regions and the corresponding interface wavelength (*IWL*), which here is quantified by the average time between leading edges of two near turbulent regions at a fixed y location. This time displacement is then transformed to a spatial wavelength through Taylor's hypothesis. Since the frequency of external intermittency was y-dependent, the y location selected for defining *IWL* was the location with the most probable interface location, i.e. the location with the highest frequency of intermittent occurrences. From the current data, this location was identified to be at $y \approx 0.7\delta$, which is close to the most probable interface location suggested by Chauhan *et al.* (2014). We thus define *IWL* as the average distance between leading edges of two near turbulent regions at $y \approx 0.7\delta$. Note that since the turbulent detection function (2.1) was low-pass filtered, *IWL* is constrained to $\gtrsim 0.5\delta$, resulting in small-scale nibbling motions being neglected.

It was found that *IWL* is nearly constant, with values between 2.38δ and 2.49δ detected for all Re_τ cases of the HRNBLWT and HRTF data sets. This is consistent with the 2δ–3δ scales attributed to outer layer bulges, and these motions being coupled with the boundary layer thickness.
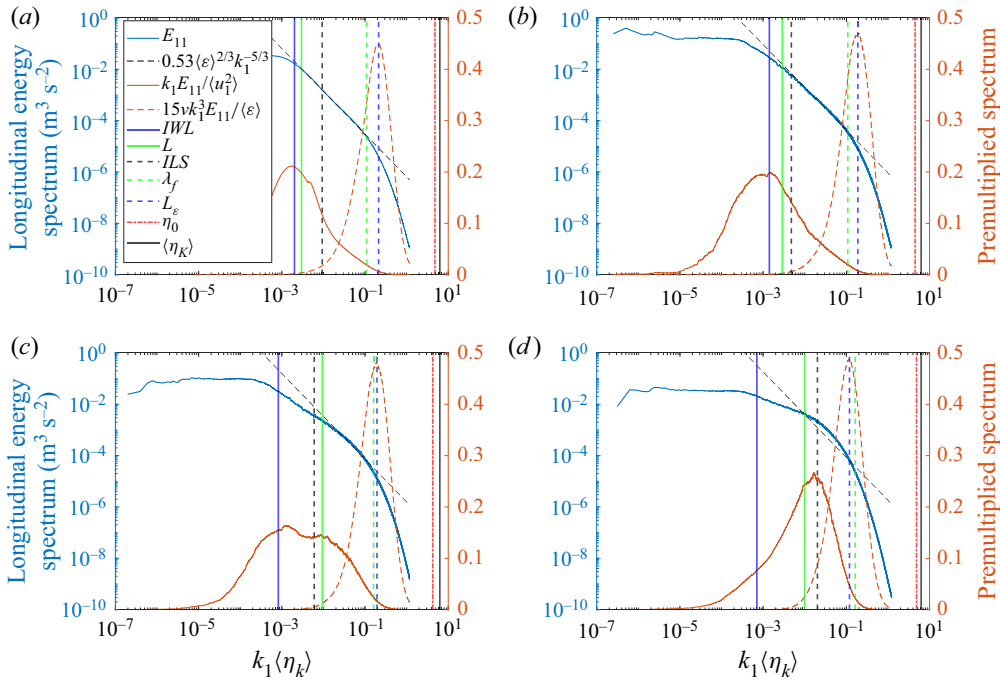
965 A17-16

Figure 7. Example longitudinal one-dimensional energy spectra (E_{11}), premultiplied longitudinal one-dimensional energy spectra ($k_1 E_{11}$), and estimated premultiplied dissipation spectra ($15 \nu k_1^3 E_{11}$). Results are shown for HRNBLWT data taken at $Re_\tau = 9500$ for four different wall-normal locations: (*a*) $y^+ = 4580$, $y/\delta \approx 0.46$; (*b*) $y^+ = 1006$, $y/\delta \approx 0.1$; (*c*) $y^+ = 95$, $y/\delta \approx 0.01$; and (*d*) $y^+ = 10$, $y/\delta \approx 0.001$. Vertical lines indicate wavenumbers corresponding to scales indicated in the legend.

4. Connection between scales and features of the wavenumber spectrum

In the previous section, we examined the wall-normal scaling of several characteristic length scales: outer-scaled parameters *ILS*, *L* and *IWL*, which depend on δ, describing large-scale flow features; inner-scaled parameters L_ε, η_0 and $\langle \eta_K \rangle$, which describe the dissipative motions; and intermediate length scale λ_f. In this section, we examine these scales in the wavenumber domain, and examine their relationship to commonly observed spectral features – specifically, the most energetic motions and the inertial subrange boundaries.

Figure 7 presents three different wavenumber spectrum representations: one-dimensional longitudinal energy spectrum $E_{11}(k_1 \langle \eta_K \rangle)$, premultiplied longitudinal energy spectrum $k_1 E_{11}(k_1 \langle \eta_K \rangle)$, and the premultiplied dissipation spectrum approximation of $15 \nu k_1^3 E_{11}$ $(k_1 \langle \eta_K \rangle)$. These spectra are examined for four wall-normal distances (i.e. different Re_L) from the $Re_\tau = 9500$ measurements taken in the HRNBLWT turbulent boundary layer. Note that the other cases showed similar results.

Interestingly, in the region where external intermittency is prominent (figure 7*a*), the average spectrum calculated from individual spectra measured in discrete turbulent regions displays a clearly identifiable, well-developed inertial subrange $E_{11} \propto k_1^{-5/3}$. This is consistent with the scale separation ($L \gg \langle \eta_K \rangle$ is approximately 3–4 orders of magnitude). The inertial subrange is bounded by $L \approx IWL$ at its low-wavenumber end, and by λ_f at its high-wavenumber end. In contrast to L and *IWL*, *ILS* lies in the inertial subrange and

965 A17-17

does not correspond to any clearly identifiable spectral feature. As expected, L_ε is smaller than λ_f, with the latter being a good representation of the upper bound of the inertial subrange. Hence despite being an average formed from intermittent turbulent regions, this longitudinal energy spectrum exhibits classical high-Reynolds-number energy spectrum characteristics. The exception is at the low-wavenumber end of the spectrum, which is under-resolved due to the variable lengths of the turbulent regions acting as a high-pass filter during the averaging process. Thus the shorter lengths of the turbulent regions do not contain any low-wavenumber information, consistent with its dependence on *IWL*.

At measurement locations closer to the wall, where external intermittency is not present, the energy-containing range is extended due to the ability to resolve much longer wavelengths (see figures 7*b*–*d*). However, the peak in the energy-containing range still corresponds closely to the scales associated with *IWL*.

Additionally, it was found that *IWL* is a good approximation of the wavelength associated with the peak of the premultiplied energy spectrum $E_{11}k_1$ for $y^+ > 200$, as can be seen in figures 7(*a*,*b*). Closer to wall, the effect of the turbulent/non-turbulent interface disappears due to the increased importance of viscous forces.

At $y^+ \approx 1000$, $y/\delta \approx 0.1$ (figure 7*b*), the high-Reynolds-number characteristics remain similar to those of figure 7(*a*), with *IWL* representing the energy-containing eddies, L representing the low-wavenumber boundary of the inertial subrange, λ_f representing the high-wavenumber boundary, and the peak dissipation occurring at scales smaller than λ_f.

As shown in figures 7(*b*–*d*), as the wall is approached, L continues to closely approximate the low-wavenumber end of the inertial subrange, decreasing faster than $\langle \eta_K \rangle$ (e.g. as shown by comparison of figures 1*d* and 3*c*), and the local separation of scales reduces. Hence the wavenumber range of the inertial subrange decreases, and the local slope of energy spectra between the wavenumbers corresponding to L and λ_f deviates significantly from $0.53\langle \varepsilon \rangle^{2/3} k_1^{-5/3}$, producing energy content above this inertial subrange description.

Once an inertial subrange is no longer evident, as in figure 7(*c*), the premultiplied spectrum exhibits the multiple modes corresponding to large-scale and very-large-scale motions. Interestingly, this also corresponds to the decrease in L, and corresponding separation of *IWL* and L, such that *IWL* corresponds to the low-wavenumber peak in the premultiplied spectrum, and L corresponds to the high-wavenumber peak. At the high-wavenumber end of the spectrum, λ_f becomes closer to L_ε, and no longer appears to correspond to the E_{11} roll-off associated with the low-wavenumber boundary of the dissipation range.

Very near the wall, as shown in figure 7(*d*), the shift in λ_f with respect to L_ε continues, and λ_f becomes smaller than L_ε, i.e. it describes scales smaller than those at which peak dissipation occurs. The variability of λ_f within the dissipation range highlights the care that should be taken when interpreting λ_f as a physical turbulence scale (Tennekes & Lumley 1972), at least when Re_L is not large enough to produce an inertial subrange. Furthermore, L and *IWL* no longer correspond to peaks in the premultiplied spectrum, as there is significant energy at scales smaller than L.

Noting that L corresponds closely to the low-wavenumber limit of the inertial subrange, *IWL* corresponds to the scales of the most energetic eddies, and L_ε corresponds to the scales at which the highest rate of dissipation occurs, we now examine scaling the relationship of the scale separation described by $L/\langle \eta_K \rangle$, IWL/L_ε, and that described by Re_τ. The ratios of these different quantities are presented as functions of wall-normal distance in figure 8.
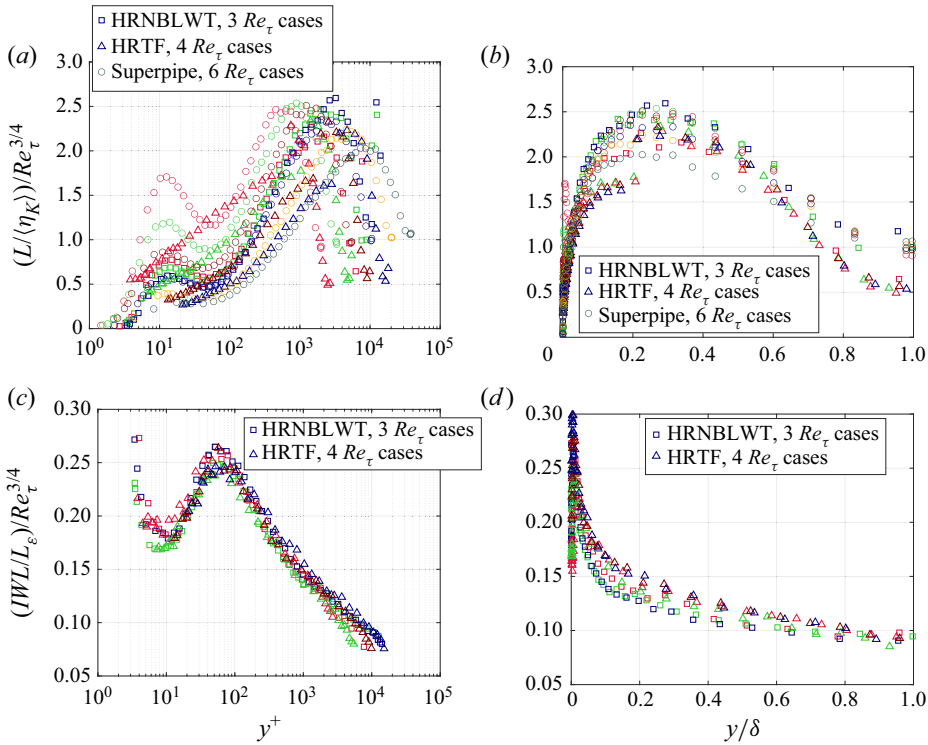
Figure 8. Profiles of $(L/\langle\eta_K\rangle)/Re_\tau^{3/4}$ as functions of (*a*) y^+ and (*b*) y/δ, along with corresponding profiles of $(IWL/L_\varepsilon)/Re_\tau^{3/4}$ as functions of (*c*) y^+ and (*d*) y/δ. Results are for all turbulent boundary layer cases, with symbols as provided in tables 1–3.

Figures 8(*a*) and 8(*b*) show the ratio $(L/\langle\eta_K\rangle)/Re_\tau^{3/4}$ as functions of y^+ and y/δ, respectively. Although there does not appear to be any consistency in y^+, the y/δ dependence is consistent throughout all cases. Figure 8(*b*) also suggests that the largest inertial subrange can be expected at $y/\delta \approx 0.3$.

Although $L/\langle\eta_K\rangle$ appears to scale only with y/δ, $(L_\varepsilon/IWL)/Re_\tau^{3/4}$ showed both y^+ and y/δ dependence (figures 8(*c*) and 8(*d*), respectively). These results indicate that the scale separation between peaks of premultiplied energy and dissipation spectra is a unique function of Re_τ and y. It should be noted, however, that since IWL and Re_τ are constant for a given profile, the wall-normal dependence shown in figures 8(*c*) and 8(*d*) is ultimately the wall-normal dependence of L_ε and a restructuring of the wall-distance dependence shown in figure 6(*a*). Interestingly, though, figure 8(*d*) suggests that through measurement of a longitudinal spectrum at a known y and δ, it is possible to recover u_τ. This is because the spectral measurement allows determination of L_ε, and given that $IWL \approx 2.45\delta$, Re_τ (and hence u_τ) can be determined from the curve shown in figure 8(*d*).

5. Conclusion

The Reynolds number and wall-normal dependencies of different turbulence length scales in pipe flow and zero-pressure-gradient boundary layer flow were investigated over a Reynolds number range spanning an order of magnitude. We examined: outer-scaled parameters L, ILS and IWL, which depend on δ, and describe large-scale flow features;

inner-scaled parameters η_0, $\langle \eta_K \rangle$ and L_ε, which describe the dissipative motions; and the intermediate length scale λ_f.

The results show that, following a correction for external intermittency, the large-scale length scale L that is characteristic of the low-wavenumber end of the inertial subrange (the start of the universal part of the spectrum) was independent of boundary conditions and depends only on the outer-scaled distance from the wall. Conversely, the integral length scale *ILS*, often conflated with the length scale of most energetic eddies, did not follow either inner or outer scaling for either pipe or boundary layer flows.

Clearly, there is a fundamental difference between these two scales, in that L assumes universal equilibrium range behaviour within its definition, whereas *ILS* covers a wide range of anisotropic, non-universal wavenumbers. The length scale *IWL*, representing the wavelength of the external intermittency, was found to correspond closely to the low-wavenumber peak in premultiplied longitudinal energy spectra for $y^+ > 200$.

Following a similar examination, the dissipative motions were found to obey inner scaling, with the same y^+ dependence regardless of boundary conditions or Reynolds number. This was the case for the classical Kolmogorov length scale $\langle \eta_K \rangle$, the dissipation length scale that accounts for internal intermittency η_0, and their respective probability density functions. The length scale L_ε, representing the scale at which the maximum rate of dissipation occurs, also obeyed inner scaling for all $y < \delta$. When coupled with $\langle \eta_K^+ \rangle$, L_ε^+ provides a robust description of the wall-normal dependence of the high-wavenumber dissipation range in the longitudinal spectrum.

Finally, the scale separation between the energy-containing eddies described by L and the dissipative scales described by $\langle \eta_K \rangle$ was found to be independent of boundary conditions, and a unique function of Re_τ and y/δ. Conversely, for the turbulent boundary layer cases, the scale separation described by *IWL* and L_ε was found to be described uniquely by Re_τ and y^+ for $y^+ < 0.5Re_\tau$, or y/δ for $y/\delta > 0.001$.

These results suggest that suitable selection of scaling arguments can be used to describe different features of the one-dimensional turbulence spectrum regardless of boundary conditions. Descriptions of the large- and small-scale wall-dependence can be leveraged potentially to improve the application of large-eddy simulation, for example by providing guidance on required mesh resolution near the wall for wall-resolved methods, or providing guidance when selecting filter cutoff values by providing scales that can guide longitudinal spectrum models, or provide estimates of where scale separation is sufficient to assume an inertial subrange. Alternatively, information about dissipation scale distributions can be used to develop small-scale forcing models used for implicit large-eddy simulations.

Declaration of interests. The authors report no conflict of interest.

Author ORCIDs.

Alexander J. Smits https://orcid.org/0000-0002-3883-8648;

Sean C.C. Bailey https://orcid.org/0000-0002-9807-9858.

REFERENCES

ALHAMDI, S.F.H. & BAILEY, S.C.C. 2017 Universality of local dissipation scales in turbulent boundary layer flows with and without free-stream turbulence. *Phys. Fluids* **29** (11), 115103.

ALHAMDI, S.F.H. & BAILEY, S.C.C. 2018 External intermittency compensation of dissipation scale distributions in a turbulent boundary layer. *Phys. Rev. Fluids* **3** (7), 074601.

BAILEY, S.C.C., HULTMARK, M., SCHUMACHER, J., YAKHOT, V. & SMITS, A.J. 2009 Measurements of the dissipation scales in turbulent pipe flow. *Phys. Rev. Lett.* **103**, 014502.

BAILEY, S.C.C., KUNKEL, G.J., HULTMARK, M., VALLIKIVI, M., HILL, J.P., MEYER, K.A., TSAY, C., ARNOLD, C.B. & SMITS, A.J. 2010 Turbulence measurements using a nanoscale thermal anemometry probe. *J. Fluid Mech.* **663**, 160–179.

BAILEY, S.C.C., VALLIKIVI, M., HULTMARK, M. & SMITS, A.J. 2014 Estimating the value of von Kármán's constant in turbulent pipe flow. *J. Fluid Mech.* **749**, 79–98.

BAILEY, S.C.C. & WITTE, B.M. 2016 On the universality of local dissipation scales in turbulent channel flow. *J. Fluid Mech.* **786**, 234–252.

BALAKUMAR, B.J. & ADRIAN, R.J. 2007 Large- and very-large-scale motions in channel and boundary-layer flows. *Phil. Trans. R. Soc.* A **365**, 665–681.

BATCHELOR, G.K. & TOWNSEND, A.A. 1949 The nature of turbulent motion at large wave-numbers. *Proc. R. Soc. Lond.* A **199**, 238–255.

CHAUHAN, K., PHILIP, J., DE SILVA, C.M., HUTCHINS, N. & MARUSIC, I. 2014 The turbulent/non-turbulent interface and entrainment in a boundary layer. *J. Fluid Mech.* **742**, 119–151.

COLES, D. 1956 The law of the wake in the turbulent boundary layer. *J. Fluid Mech.* **1**, 191–226.

CORRSIN, S. & KISTLER, A.L. 1955 Free-stream boundaries of turbulent flows. *Tech. Rep.* Johns Hopkins University.

DEL ÁLAMO, J.C. & JIMÉNEZ, J. 2009 Estimation of turbulent convection velocities and corrections to Taylor's approximation. *J. Fluid Mech.* **640**, 5–26.

FIEDLER, H. & HEAD, M.R. 1966 Intermittency measurements in the turbulent boundary layer. *J. Fluid Mech.* **25** (4), 719–735.

GRANT, H.L., STEWART, R.W. & MOILLIET, A. 1962 Turbulence spectra from a tidal channel. *J. Fluid Mech.* **12**, 241–268.

GUALA, M., HOMMEMA, S.E. & ADRIAN, R.J. 2006 Large-scale and very-large-scale motions in turbulent pipe flow. *J. Fluid Mech.* **554**, 521–542.

HAMLINGTON, P.E., KRASNOV, D., BOECK, T. & SCHUMACHER, J. 2012*a* Local dissipation scales and energy dissipation-rate moments in channel flow. *J. Fluid Mech.* **701**, 419–429.

HAMLINGTON, P., KRASNOV, D., BOECK, T. & SCHUMACHER, J. 2012*b* Statistics of the energy dissipation rate and local enstrophy in turbulent channel flow. *Physica* D **241**, 169–177.

HEAD, M.R. & BANDYOPADHYAY, P. 1981 New aspects of turbulent boundary-layer structure. *J. Fluid Mech.* **107**, 297–337.

HEDLEYT, T.B. & KEFFER, J.F. 1974 Some turbulent/non-turbulent properties of the outer intermittent region of a boundary layer. *J. Fluid Mech.* **64** (4), 645–678.

HOLZNER, M., LIBERZON, A., NIKITIN, N., KINZELBACH, W. & TSINOBER, A. 2007 Small-scale aspects of flows in proximity of the turbulent/nonturbulent interface. *Phys. Fluids* **19** (7), 071702–071702–4.

HULTMARK, M., VALLIKIVI, M., BAILEY, S.C.C. & SMITS, A.J. 2012 Turbulent pipe flow at extreme Reynolds numbers. *Phys. Rev. Lett.* **108**, 094501.

HULTMARK, M., VALLIKIVI, M., BAILEY, S.C.C. & SMITS, A.J. 2013 Logarithmic scaling of turbulence in smooth- and rough-wall pipe flow. *J. Fluid Mech.* **728**, 376–395.

HUTCHINS, N., HAMBLETON, W.T. & MARUSIC, I. 2005 Inclined cross-stream stereo particle image velocimetry measurements in turbulent boundary layers. *J. Fluid Mech.* **541**, 21–54.

JIMÉNEZ, J., HOYAS, S., SIMENS, M.P. & MIZUNO, Y. 2010 Turbulent boundary layers and channels at moderate Reynolds numbers. *J. Fluid Mech.* **657**, 335–360.

KIM, K.C. & ADRIAN, R.J. 1999 Very large-scale motion in the outer layer. *Phys. Fluids* **11** (2), 417–422.

KLINE, S.J., REYNOLDS, W.C., SCHRAUB, F.A. & RUNSTADLER, P.W. 1967 The structure of turbulent boundary layers. *J. Fluid Mech.* **30**, 741–773.

KOLMOGOROV, A.N. 1941 The local structure of turbulence in incompressible viscous fluid for very large Reynolds numbers. *Dokl. Akad. Nauk SSSR* **30**, 301–305.

KOVASZNAY, L.S.G. 1967 Structure of the turbulent boundary layer. *Phys. Fluids* **10** (9), S25–S30.

KOVASZNAY, L.G., KIBENS, V. & BLACKWELDER, R.F. 1970 Large-scale motion in the intermittent region of a turbulent boundary layer. *J. Fluid Mech.* **41** (2), 283–325.

LEE, M. & MOSER, R.D. 2015 Direct numerical simulation of turbulent channel flow up to $Re_\tau \approx 5200$. *J. Fluid Mech.* **774**, 395–415.

MARUSIC, I., MATHIS, R. & HUTCHINS, N. 2010 Predictive model for wall-bounded turbulent flow. *Science* **329**, 193–196.

MARUSIC, I., MONTY, J.P., HULTMARK, M. & SMITS, A.J. 2013 On the logarithmic region in wall turbulence. *J. Fluid Mech.* **716**, R3.

MATHEW, J. & BASU, A.J. 2002 Some characteristics of entrainment at a cylindrical turbulence boundary. *Phys. Fluids* **14** (7), 2065–2072.

MATHIS, R., HUTCHINS, N. & MARUSIC, I. 2009 Large-scale amplitude modulation of the small-scale structures in turbulent boundary layers. *J. Fluid Mech.* **628**, 311–337.

MENEVEAU, C. & SREENIVASAN, K.R. 1991 The multifractal nature of turbulent energy dissipation. *J. Fluid Mech.* **224**, 429–484.

MONKEWITZ, P.A. 2022 Asymptotics of streamwise Reynolds stress in wall turbulence. *J. Fluid Mech.* **931**, A18.

MONTY, J.P. 2005 Developments in smooth wall turbulent duct flows. PhD thesis, University of Melbourne.

MONTY, J.P., HUTCHINS, N., NG, H.C.H., MARUSIC, I. & CHONG, M.S. 2009 A comparison of turbulent pipe, channel and boundary layer flows. *J. Fluid Mech.* **632**, 431–442.

MORRISON, J.F., MCKEON, B.J., JIANG, W. & SMITS, A.J. 2004 Scaling of the streamwise velocity component in turbulent pipe flow. *J. Fluid Mech.* **508**, 99–131.

MORSHED, N.M., VENAYAGAMOORTHY, S.K. & DASI, L.P. 2013 Intermittency and local dissipation scales under strong mean shear. *Phys. Fluids* **25**, 011701.

NICKELS, T.B., MARUSIC, I., HAFEZ, S., HUTCHINS, N. & CHONG, M.S. 2007 Some predictions of the attached eddy model for a high Reynolds number boundary layer. *Phil. Trans. R. Soc.* A **365**, 807–822.

PALADIN, G. & VULPIANI, A. 1987 Degrees of freedom of turbulence. *Phys. Rev.* A **35**, 1971–1973.

PERRY, A.E., HENBEST, S. & CHONG, M.S. 1986 A theoretical and experimental study of wall turbulence. *J. Fluid Mech.* **165**, 163–199.

POPE, S.B. 2000 *Turbulent Flows*. Cambridge University Press.

ROSENBERG, B.J., HULTMARK, M., VALLIKIVI, M., BAILEY, S.C.C. & SMITS, A.J. 2013 Turbulence spectra in smooth- and rough-wall pipe flow at extreme Reynolds numbers. *J. Fluid Mech.* **731**, 46–63.

SADDOUGHI, S.G. & VEERAVALLI, S.V. 1994 Local isotropy in turbulent boundary layers at high Reynolds number. *J. Fluid Mech.* **268**, 333–372.

SADDOUGHI, S.G. & VEERAVALLI, S.V. 1996 Hot-wire anemometry behaviour at very high frequencies. *Meas. Sci. Technol.* **7**, 1297–1300.

SCHUMACHER, J., SCHEEL, J.D., KRASNOV, D., DONZIS, D.A., YAKHOT, V. & SREENIVASAN, K.R. 2014 Small-scale universality in fluid turbulence. *Proc. Natl Acad. Sci.* **111**, 10961–10965.

SCHUMACHER, J., SREENIVASAN, K.R. & YAKHOT, V. 2007 Asymptotic exponents from low-Reynolds-number flows. *New J. Phys.* **9**, 89.

DE SILVA, C.M., HUTCHINS, N. & MARUSIC, I. 2016 Uniform momentum zones in turbulent boundary layers. *J. Fluid Mech.* **786**, 309–331.

SMITS, A.J. 2020 Some observations on Reynolds number scaling in wall-bounded flows. *Phys. Rev. Fluids* **5** (11), 110514.

SMITS, A.J., HULTMARK, M., LEE, M., PIROZZOLI, S. & WU, X. 2021 Reynolds stress scaling in the near-wall region of wall-bounded flows. *J. Fluid Mech.* **926**, A31.

SMITS, A.J., MONTY, J.P., HULTMARK, M., BAILEY, S.C.C., HUTCHINS, N. & MARUSIC, I. 2011 Spatial resolution correction for wall-bounded turbulence measurements. *J. Fluid Mech.* **676**, 41–53.

SREENIVASAN, K.R. 1995 On the universality of the Kolmogorov constant. *Phys. Fluids* **7** (11), 2778–2784.

TAYLOR, G.I. 1938 The spectrum of turbulence. *Proc. R. Soc. Lond.* **164** (919), 476–490.

TENNEKES, H. & LUMLEY, J.L. 1972 *A First Course in Turbulence*. The MIT Press.

TOMKINS, C.D. & ADRIAN, R.J. 2005 Energetic spanwise modes in the logarithmic layer of a turbulent boundary layer. *J. Fluid Mech.* **545**, 141–162.

TOWNSEND, A.A. 1976 *The Structure of Turbulent Shear Flow*. Cambridge University Press.

TSUJI, Y., HONDA, K., NAKAMURA, I. & SATO, S. 1991 Is intermittent motion of outer flow in the turbulent boundary layer deterministic chaos? *Phys. Fluids* A*: Fluid Dyn.* **3** (8), 1941–1946.

VALLIKIVI, M., GANAPATHISUBRAMANI, B. & SMITS, A.J. 2015a Spectral scaling in boundary layers and pipes at very high Reynolds numbers. *J. Fluid Mech.* **771**, 303–326.

VALLIKIVI, M., HULTMARK, M., BAILEY, S.C.C. & SMITS, A.J. 2011 Turbulence measurements in pipe flow using a nano-scale thermal anemometry probe. *Exp. Fluids* **51**, 1521–1527.

VALLIKIVI, M., HULTMARK, M. & SMITS, A.J. 2015b Turbulent boundary layer statistics at very high Reynolds number. *J. Fluid Mech.* **779**, 371–389.

VALLIKIVI, M. & SMITS, A.J. 2014 Fabrication and characterization of a novel nanoscale thermal anemometry probe. *J. Microelectromech. Syst.* **23** (4), 899–907.

WESTERWEEL, J., FUKUSHIMA, C., PEDERSEN, J.M. & HUNT, J.C.R. 2005 Mechanics of the turbulent-nonturbulent interface of a jet. *Phys. Rev. Lett.* **95**, 174501; Erratum *Phys. Rev. Lett.* **95**, 199902.

YAKHOT, V. 2006 Probability densities in strong turbulence. *Physica* D **215** (2), 166–174.

YAKHOT, V., BAILEY, S.C.C. & SMITS, A.J. 2010 Scaling of global properties of turbulence and skin friction in pipe and channel flows. *J. Fluid Mech.* **652**, 65–73.

ZAMAN, K.B.M.Q. & HUSSAIN, A.K.M.F. 1981 Taylor hypothesis and large-scale coherent structures. *J. Fluid Mech.* **112**, 379–396.

ZHOU, Q. & XIA, K.-Q. 2010 Universality of local dissipation scales in buoyancy-driven turbulence. *Phys. Rev. Lett.* **104** (12), 124301.